Nanoscale

PAPER

View Article Online
View Journal | View Issue

Exciton diffusion in monolayer and bulk $MoSe_2$†

Cite this: *Nanoscale*, 2014, **6**, 4915

Nardeep Kumar,[a] Qiannan Cui,[a] Frank Ceballos,[a] Dawei He,[b] Yongsheng Wang*[b] and Hui Zhao*[a]

Received 3rd January 2014
Accepted 20th February 2014

DOI: 10.1039/c3nr06863c

www.rsc.org/nanoscale

The exciton dynamics in monolayer and bulk $MoSe_2$ samples are studied by transient absorption microscopy with a high spatiotemporal resolution. Excitons are injected with a point-like spatial distribution using a tightly focused femtosecond pulse. The spatiotemporal dynamics of these excitons are monitored by measuring transient absorption of a time-delayed and spatially scanned probe pulse. We obtain the exciton diffusion coefficients of 12 ± 3 and 19 ± 2 $cm^2\ s^{-1}$ and exciton lifetimes of 130 ± 20 and 210 ± 10 ps in the monolayer and bulk samples, respectively. These values are useful for understanding excitons and their interactions with the environment in these structures and potential applications of $MoSe_2$ in optoelectronics and electronics.

1 Introduction

Recently, semiconducting transition metal dichalcogenides, MX_2 (M = Mo, W; X = S, Se, Te), have drawn considerable interest, stimulated by successful fabrication of the two-dimensional (2D) crystals containing a few or single atomic layers.[1,2] These 2D crystals have shown several exotic properties, such as transition to a direct bandgap in monolayers,[3,4] valley selective optical coupling,[5–11] extremely large binding energies of excitons, trions, and biexcitons,[12,13,41] and large nonlinear optical responses.[14–17] Based on these properties, various applications of MX_2 2D crystals have been developed, including transistors,[18–20] phototransistors,[21,22] chemical sensors,[23] light-emitting diodes,[24] and light modulators.[25]

So far, most efforts have been concentrated on one member of this family, MoS_2. However, $MoSe_2$, with a similar structure, possesses several properties that make it attractive too. For example, its direct bandgap of 1.55 eV is close to the optimal bandgap value of single-junction photovoltaic devices. Several studies have demonstrated applications of $MoSe_2$ in photovoltaics[26,27] and photocatalysis.[28] Few-layer $MoSe_2$ has nearly degenerate direct and indirect bandgaps. Hence, it is possible to control and even modulate the nature of the bandgap, and therefore its optical properties, by temperature[29] and strain.[29,30] From a broader perspective, it was proposed that these 2D crystals can be used as building blocks to fabricate new van der Waals heterostructures and even new 3D crystals.[31–33] Very recently, such structures have been fabricated and investigated for applications in photovoltaics,[34,35] vertical field-effect tunneling transistors,[36,37] and memory devices.[38,39] $MoSe_2$ can play an important role in this new way of material design and discovery. Indeed, the growth of monolayer $MoSe_2$ on MoS_2 by molecular beam epitaxy was achieved a long time ago.[40]

Because of the unusually large exciton binding energies in these 2D crystals, their optical properties are dominated by excitons even at room temperature. In particular, real-space transport and recombination of excitons play important roles in optoelectronic applications. Although a recent time-integrated photoluminescence experiment demonstrated electrical control of neutral and charged excitons,[13] the exciton dynamics has not been studied in neither monolayer nor bulk $MoSe_2$. Here we report a study of exciton dynamics in monolayer and bulk $MoSe_2$ by femtosecond transient absorption microscopy. The high spatiotemporal resolution allows us to directly measure the exciton diffusion coefficient and lifetime. These results provide fundamental parameters for understanding excitons in these structures.

2 Experimental section

Samples of monolayer $MoSe_2$ are fabricated by mechanical exfoliation with an adhesive tape from bulk crystals. By depositing flakes of $MoSe_2$ on silicon substrates with a 90 nm SiO_2 layer, we can identify thin layers of $MoSe_2$ with an optical microscope, by utilizing optical contrasts enhanced by the multilayer substrate.[42,43] The inset of Fig. 1 shows the microscopy picture of a large and isolated flake used in this study. The contrast of the flake with respect to the substrate is consistent with the monolayer thickness.[42,43] Under excitation of a 632.8 nm laser beam, strong photoluminescence with a central wavelength of 788 nm is observed, as shown by the red curve in

[a]*Department of Physics and Astronomy, The University of Kansas, Lawrence, Kansas 66045, USA. E-mail: huizhao@ku.edu; Fax: +1 785 864 5262; Tel: +1 785 864 1938*

[b]*Key Laboratory of Luminescence and Optical Information, Ministry of Education, Institute of Optoelectronic Technology, Beijing Jiaotong University, Beijing 100044, China*

† Electronic supplementary information (ESI) available: Relationship between the differential reflection, the differential absorption, and the exciton density; drift diffusion model and fits to the exciton density profiles. See DOI: 10.1039/c3nr06863c

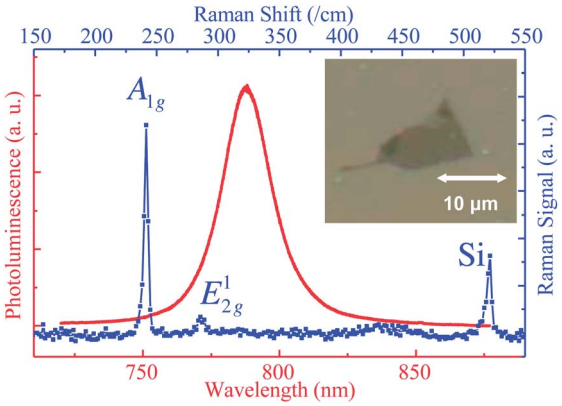

Fig. 1 Photoluminescence (red, left and bottom axes) and Raman (blue, right and top axes) spectra of the monolayer $MoSe_2$ flake used for the study, which is shown in the inset.

Fig. 1, which is consistent with recently reported photoluminescence peak wavelengths in the range of 784–794 nm.[13,29,44] The linewidth is about 22 nm, which is also in the range of the recently reported values of 15–50 nm.[13,44] The blue curve in Fig. 1 (top and right axes) shows a Raman spectrum of the sample, with two peaks at 242 and 286 cm^{-1}, corresponding to the A_{1g} and E^1_{2g} phonon modes of monolayer $MoSe_2$, respectively. These values, as well as the ratio of the peak heights of about 13, are reasonably consistent with the reported results of monolayer $MoSe_2$.[29,44–47]

In the transient absorption microscopy setup, as shown schematically in Fig. 2, an 80 MHz mode-locked Ti:sapphire laser (Ti:Sa) is used to generate 100 fs pulses with a central wavelength of 810 nm. The majority of this beam is used to pump an optical parametric oscillator (OPO), which has a signal output of 1500 nm. To obtain the pump pulse for the measurement, a beta barium borate (BBO) crystal is used to generate the second harmonic of this beam, with a wavelength of 750 nm. It is focused to a spot size of about 1 μm using a microscope objective lens. The pump pulse is tuned to the high-energy edge of the A-exciton resonance (Fig. 1); hence, it resonantly injects excitons. A small portion of the Ti:Sa output is used as the probe and is focused to the sample by the same objective lens. The reflected probe is collimated by the objective lens and is sent to one detector of a balanced detector. Color filters are used in front of the detector to block the unwanted

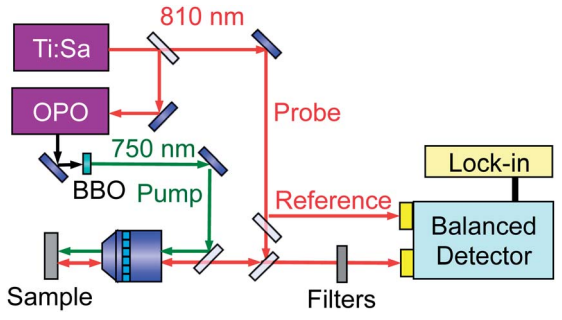

Fig. 2 Schematics of the transient absorption microscopy setup.

light. Before entering the sample, a portion of the probe is reflected to another detector of the balanced detector, as a reference beam, in order to suppress the common-mode laser intensity noise.

The balanced detector outputs a voltage that is proportional to the difference between optical powers on the two detectors. Without the presence of the pump, we adjust the power of the reference to match that of the probe, such that the balanced detector outputs a zero voltage. With the presence of the pump, the probe power reaching the detector changes, owing to the change in the reflection coefficient of the sample caused by the pump-injected excitons. The balanced detector outputs a voltage that is proportional to the differential reflection of the probe, which is defined as the relative change of the reflection of the probe, $\Delta R/R_0 = (R - R_0)/R_0$, where R and R_0 are the reflection coefficients of the sample at the probe wavelength, with and without the presence of the pump pulse, respectively. This output is measured using a lock-in amplifier referenced to a mechanical chopper in the pump arm. To measure the differential reflection as a function of the probe delay, we change the length of the pump arm by moving a retroreflector in the pump arm (not shown). The probe spot is scanned with respect to the pump spot by tilting a beamsplitter that reflects the probe beam into the objective lens.

The total reflection of the probe is determined by the reflection from the sample surface and from the interfaces of sample–SiO_2 and SiO_2–Si. Consequently, the differential reflection is related to changes of the complex index of refraction of $MoSe_2$ induced by the excitons injected by the pump pulse. Strictly speaking, the relationship between the differential reflection and the exciton density can be complex and often non-analytical. However, for low exciton densities and small magnitudes of differential reflection, the relationship is often linear. For our purpose of monitoring exciton dynamics with differential reflection, we verify that the differential reflection is proportional to the exciton density by measuring the differential reflection at early probe delays as a function of the pump fluence. With the known absorption coefficient at the pump wavelength,[48] we deduce the injected exciton density from the pump fluence by using Beer's law and assuming that each absorbed photon creates one exciton. We find that a differential reflection of 10^{-4} corresponds to an area exciton density of 10^{11} cm^{-2}. We use this relationship to convert the measured differential reflection into the exciton density. We note that any uncertainties in this process merely change the absolute value of the labeled exciton densities and would not influence our discussions on exciton dynamics.

3 Results and discussion

We spatially and temporally resolve the excitonic dynamics by measuring the differential reflection as we scan the probe spot with respect to the pump spot at various probe delays. Fig. 3(a) shows the deduced exciton density as a function of time and space. The zero probe location is defined where the centers of the probe and pump spots overlap. To analyze the broadening of the profiles, we fit the profiles at different probe delays by

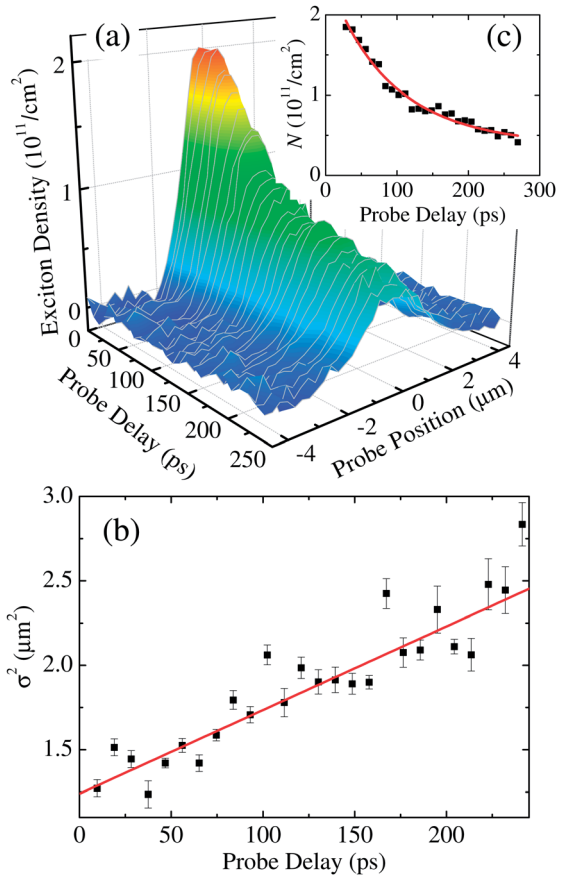

Fig. 3 (a) Spatiotemporal dynamics of exciton in monolayer $MoSe_2$. (b) Square widths of the profiles at various probe delays determined by Gaussian fits to the profiles shown in (a). The red line is a linear fit. (c) The exciton density measured at the zero probe position as a function of probe delay. The red line is a fit that includes contributions of both the recombination and the diffusion.

Gaussian functions to determined their $1/e$ widths (σ). The results are plotted in Fig. 3(b). A significant broadening of the profile can be seen, which is caused by diffusion of excitons out of the excitation region.

The spatiotemporal dynamics of the injected excitons can be described using the diffusion equation.[49] With a Gaussian initial profile, the profile remains Gaussian with the width evolving as $\sigma^2(t) = \sigma_0^2 + 4Dt$, where D and σ_0 are the diffusion coefficient and the width of the initial density profile at $t = 0$, respectively. By fitting the data with this equation, as shown by the red line in Fig. 3(b), we deduce a diffusion coefficient of 12 ± 3 cm^2 s^{-1}. We note that this procedure to measure the diffusion coefficient is not influenced by the decay of the overall exciton density due to the exciton recombination, which does not change the width. Furthermore, the finite probe spot size does not influence the measurement either, since it merely adds a constant to all the squared widths and hence does not change the slope.

The spatiotemporal resolution of the exciton density also allows us to measure the exciton lifetime. Fig. 3(c) shows the measured exciton density as a function of probe delay with the centers of the probe and pump spots overlapping ($x = 0$). The decrease of the exciton density is caused by both the diffusion and the exciton recombination. Considering the probe spot is Gaussian with a finite size, σ_p, it is straightforward to show that the exciton density is $N(x = 0) \propto \frac{1}{\sigma_p^2 + \sigma_0^2 + 4Dt} \exp\left[\frac{-t}{\tau}\right]$. We fit the data shown in Fig. 3(c) with this equation, with the known value of D, and find a satisfactory agreement [red curve in Fig. 3(c)]. We deduce an exciton lifetime of 130 ± 20 ps.

The measured exciton diffusion coefficient and lifetime reveal fundamental interactions between excitons and their environment in $MoSe_2$ monolayers. From these values, we deduce a diffusion length ($\sqrt{D\tau}$) of about 400 nm and a mean free time (D/v_T^2, where v_T is the thermal velocity) of about 0.2 ps. The study of exciton transport can also provide insight into charge transport properties in $MoSe_2$, which are important for various electronic applications. From the Einstein relationship, we obtain an exciton mobility of $\mu = eD/k_BT \sim 480$ cm^2 V^{-1} s^{-1}, where e, k_B, and T are the elementary charge, Boltzmann constant, and temperature, respectively. This value is about one order of magnitude higher than the electron mobility of about 50 cm^2 V^{-1} s^{-1} in a seven-layer flake of $MoSe_2$ obtained in a recent transport measurement.[19] We note that the exciton mobility is related to, but different from, the charge mobilities. Excitons are neutral particles, and therefore their interactions with charged impurities and piezoelectric types of phonons are weaker than those with charge carriers.

We repeat the measurement on a thick flake fabricated from the same crystal and on the same substrate. The exact number of atomic layers is unknown; however, because it is not transparent, its thickness is at least several hundreds of nanometers. Since the penetration depth of the pump pulse is about 50 nm, it can be safely treated as a bulk sample. Fig. 4 summarizes the results from this bulk sample, in the same fashion as Fig. 3. By analyzing these data, we obtain a diffusion coefficient and a lifetime of 19 ± 2 cm^2 s^{-1} and 210 ± 10 ps, respectively. These values correspond to a diffusion length of about 600 nm, a mean free time of about 0.3 ps, and an exciton mobility of about 730 cm^2 V^{-1} s^{-1}. Previously, charge mobilities on the order of 100 cm^2 V^{-1} s^{-1} have been measured in bulk $MoSe_2$.[50] Furthermore, an earlier photoemission measurement yielded an interlayer diffusion coefficient on the order of 1 cm^2 s^{-1}.[51] The significantly faster intralayer diffusion observed here illustrates the anisotopic transport property of this layered material.

By comparing our results of monolayer and bulk $MoSe_2$, we note that the quantum confinement in monolayer $MoSe_2$ does not change the exciton diffusion coefficient dramatically, despite its significant impact on the nature of the bandgap and the optical properties. This is, however, consistent with previous electrical measurements on MoS_2, where similar mobilities were obtained in flakes with different thicknesses.[18] We suggest that the slightly smaller diffusion coefficient in monolayer $MoSe_2$ is due to additional scattering mechanisms from the substrate. To fully understand this, measurements on monolayer samples that are either suspended or on other types

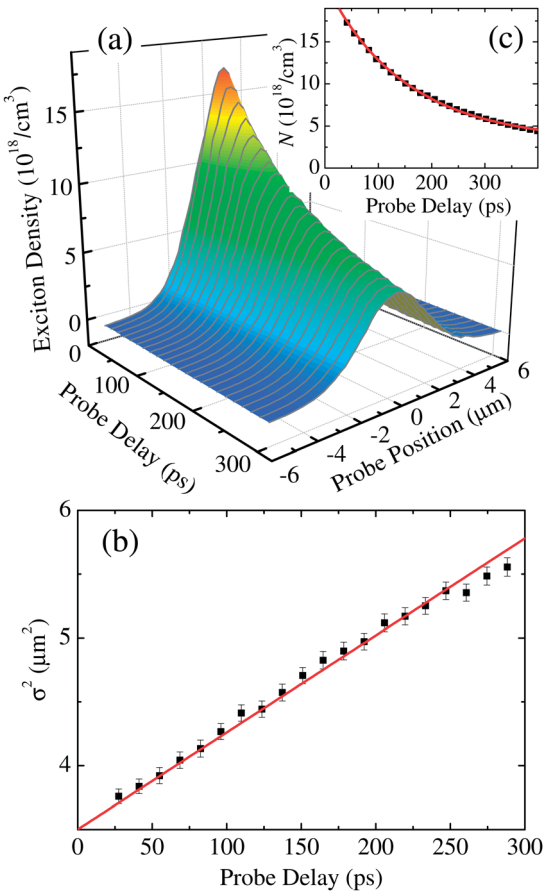

Fig. 4 (a) Spatiotemporal dynamics of exciton in bulk $MoSe_2$. (b) Square widths of the profiles at various probe delays determined by Gaussian fits to the profiles shown in (a). The red line is a linear fit. (c) The exciton density measured at the zero probe position as a function of probe delay. The red line is a fit that includes contributions of both the recombination and the diffusion.

of substrates are desired. Furthermore, the shorter lifetime in monolayer $MoSe_2$ can be attributed to the enhanced recombination due to the direct bandgap.

4 Conclusions

In summary, we performed the first time-resolved study on exciton dynamics in monolayer and bulk $MoSe_2$. We obtained exciton lifetimes of 130 ± 20 and 210 ± 10 ps in the monolayer and bulk samples, respectively. The shorter lifetime in monolayer $MoSe_2$ reflects the recombination enhancement due to its direct bandstructure. By time resolving the evolution of the exciton density profiles, we directly measured diffusion coefficients of 12 ± 3 and 19 ± 2 cm^2 s^{-1} in the monolayer and bulk samples, respectively. Using these results, we further deduced other important parameters of excitons, such as the diffusion length, the mobility, and the mean free time. These parameters are important for understanding excitons and their interactions with the environment in these structures, and potential applications of $MoSe_2$ in optoelectronics and electronics.

Acknowledgements

H.Z. acknowledges support from the US National Science Foundation under Award no. DMR-0954486. D.H. and Y.W. acknowledge supports from the National Basic Research Program 973 of China (2011CB932700 and 2011CB932703), Chinese Natural Science Foundation (61335006, 61378073, and 61077044), and Beijing Natural Science Foundation (4132031).

References

1 K. S. Novoselov, D. Jiang, F. Schedin, T. J. Booth, V. V. Khotkevich, S. V. Morozov and A. K. Geim, *Proc. Natl. Acad. Sci. U. S. A.*, 2005, **102**, 10451–10453.
2 J. N. Coleman, M. Lotya, A. O'neill, S. D. Bergin, P. J. King, U. Khan, K. Young, A. Gaucher, S. De, R. J. Smith, I. V. Shvets, S. K. Arora, G. Stanton, H.-Y. Kim, K. Lee, G. T. Kim, G. S. Duesberg, T. Hallam, J. J. Boland, J. J. Wang, J. F. Donegan, J. C. Grunlan, G. Moriarty, A. Shmeliov, R. J. Nicholls, J. M. Perkins, E. M. Grieveson, K. Theuwissen, D. W. McComb, P. D. Nellist and V. Nicolosi, *Science*, 2011, **331**, 568–571.
3 K. F. Mak, C. Lee, J. Hone, J. Shan and T. F. Heinz, *Phys. Rev. Lett.*, 2010, **105**, 136805.
4 A. Splendiani, L. Sun, Y. Zhang, T. Li, J. Kim, C. Y. Chim, G. Galli and F. Wang, *Nano Lett.*, 2010, **10**, 1271–1275.
5 D. Xiao, G. B. Liu, W. Feng, X. Xu and W. Yao, *Phys. Rev. Lett.*, 2012, **108**, 196802.
6 H. Zeng, J. Dai, W. Yao, D. Xiao and X. Cui, *Nat. Nanotechnol.*, 2012, **7**, 490–493.
7 K. F. Mak, K. He, J. Shan and T. F. Heinz, *Nat. Nanotechnol.*, 2012, **7**, 494–498.
8 A. M. Jones, H. Yu, N. J. Ghimire, S. Wu, G. Aivazian, J. S. Ross, B. Zhao, J. Yan, D. G. Mandrus, D. Xiao, W. Yao and X. Xu, *Nat. Nanotechnol.*, 2013, **8**, 634–638.
9 T. Cao, G. Wang, W. P. Han, H. Q. Ye, C. R. Zhu, J. R. Shi, Q. Niu, P. H. Tan, E. Wang, B. L. Liu and J. Feng, *Nat. Commun.*, 2012, **3**, 887.
10 Z. Gong, G.-B. Liu, H. Yu, D. Xiao, X. Cui, X. Xu and W. Yao, *Nat. Commun.*, 2013, **4**, 2053.
11 S. Wu, J. S. Ross, G.-B. Liu, G. Aivazian, A. Jones, Z. Fei, W. Zhu, D. Xiao, W. Yao, D. Cobden and X. Xu, *Nat. Phys.*, 2013, **9**, 149–153.
12 K. F. Mak, K. He, C. Lee, G. H. Lee, J. Hone, T. F. Heinz and J. Shan, *Nat. Mater.*, 2013, **12**, 207–211.
13 J. S. Ross, S. Wu, H. Yu, N. J. Ghimire, A. M. Jones, G. Aivazian, J. Yan, D. G. Mandrus, D. Xiao, W. Yao and X. Xu, *Nat. Commun.*, 2013, **4**, 1474.
14 H. Zeng, G.-B. Liu, J. Dai, Y. Yan, B. Zhu, R. He, L. Xie, S. Xu, X. Chen, W. Yao and X. Cui, *Sci. Rep.*, 2013, **3**, 1608.
15 N. Kumar, S. Najmaei, Q. Cui, F. Ceballos, P. M. Ajayan, J. Lou and H. Zhao, *Phys. Rev. B: Condens. Matter Mater. Phys.*, 2013, **87**, 161403.
16 L. M. Malard, T. V. Alencar, A. P. M. Barboza, K. F. Mak and A. M. de Paula, *Phys. Rev. B: Condens. Matter Mater. Phys.*, 2013, **87**, 201401.

17 Y. Li, Y. Rao, K. F. Mak, Y. You, S. Wang, C. R. Dean and T. F. Heinz, *Nano Lett.*, 2013, **13**, 3329–3333.
18 B. Radisavljevic, A. Radenovic, J. Brivio, V. Giacometti and A. Kis, *Nat. Nanotechnol.*, 2011, **6**, 147–150.
19 S. Larentis, B. Fallahazad and E. Tutuc, *Appl. Phys. Lett.*, 2012, **101**, 223104.
20 W. Wu, D. De, S.-C. Chang, Y. Wang, H. Peng, J. Bao and S.-S. Pei, *Appl. Phys. Lett.*, 2013, **102**, 142106.
21 H. S. Lee, S. W. Min, Y. G. Chang, M. K. Park, T. Nam, H. Kim, J. H. Kim, S. Ryu and S. Im, *Nano Lett.*, 2012, **12**, 3695–3700.
22 W. J. Zhang, J. K. Huang, C. H. Chen, Y. H. Chang, Y. J. Cheng and L. J. Li, *Adv. Mater.*, 2013, **25**, 3456–3461.
23 F. K. Perkins, A. L. Friedman, E. Cobas, P. M. Campbell, G. G. Jernigan and B. T. Jonker, *Nano Lett.*, 2013, **13**, 668–673.
24 R. S. Sundaram, M. Engel, A. Lombardo, R. Krupke, A. C. Ferrari, P. Avouris and M. Steiner, *Nano Lett.*, 2013, **13**, 1416–1421.
25 S. Tongay, J. Zhou, C. Ataca, J. Liu, J. S. Kang, T. S. Matthews, L. You, J. B. Li, J. C. Grossman and J. Q. Wu, *Nano Lett.*, 2013, **13**, 2831–2836.
26 B. Shin, Y. Zhu, N. A. Bojarczuk, S. J. Chey and S. Guha, *Appl. Phys. Lett.*, 2012, **101**, 053903.
27 B. Shin, N. A. Bojarczuk and S. Guha, *Appl. Phys. Lett.*, 2013, **102**, 091907.
28 Y. F. Shi, C. X. Hua, B. Li, X. P. Fang, C. H. Yao, Y. C. Zhang, Y. S. Hu, Z. X. Wang, L. Q. Chen, D. Y. Zhao and G. D. Stucky, *Adv. Funct. Mater.*, 2013, **23**, 1832–1838.
29 S. Tongay, J. Zhou, C. Ataca, K. Lo, T. S. Matthews, J. B. Li, J. C. Grossman and J. Q. Wu, *Nano Lett.*, 2012, **12**, 5576–5580.
30 S. Horzum, H. Sahin, S. Cahangirov, P. Cudazzo, A. Rubio, T. Serin and F. M. Peeters, *Phys. Rev. B: Condens. Matter Mater. Phys.*, 2013, **87**, 125415.
31 A. K. Geim and I. V. Grigorieva, *Nature*, 2013, **499**, 419–425.
32 V. V. Gobre and A. Tkatchenko, *Nat. Commun.*, 2013, **4**, 2341.
33 S. J. Haigh, A. Gholinia, R. Jalil, S. Romani, L. Britnell, D. C. Elias, K. S. Novoselov, L. A. Ponomarenko, A. K. Geim and R. Gorbachev, *Nat. Mater.*, 2012, **11**, 764–767.
34 L. Britnell, R. M. Ribeiro, A. Eckmann, R. Jalil, B. D. Belle, A. Mishchenko, Y.-J. Kim, R. V. Gorbachev, T. Georgiou, S. V. Morozov, A. N. Grigorenko, A. K. Geim, C. Casiraghi, A. H. C. Neto and K. S. Novoselov, *Science*, 2013, **340**, 1311–1314.
35 W. J. Yu, Y. Liu, H. Zhou, A. Yin, Z. Li, Y. Huang and X. Duan, *Nat. Nanotechnol.*, 2013, **8**, 952–958.
36 T. Georgiou, R. Jalil, B. D. Belle, L. Britnell, R. V. Gorbachev, S. V. Morozov, Y. J. Kim, A. Gholinia, S. J. Haigh, O. Makarovsky, L. Eaves, L. A. Ponomarenko, A. K. Geim, K. S. Novoselov and A. Mishchenko, *Nat. Nanotechnol.*, 2013, **8**, 100–103.
37 L. Britnell, R. V. Gorbachev, R. Jalil, B. D. Belle, F. Schedin, A. Mishchenko, T. Georgiou, M. I. Katsnelson, L. Eaves, S. V. Morozov, N. M. R. Peres, J. Leist, A. K. Geim, K. S. Novoselov and L. A. Ponomarenko, *Science*, 2012, **335**, 947–950.
38 M. S. Choi, G. H. Lee, Y. J. Yu, D. Y. Lee, S. H. Lee, P. Kim, J. Hone and W. J. Yoo, *Nat. Commun.*, 2013, **4**, 1624.
39 K. Roy, M. Padmanabhan, S. Goswami, T. P. Sai, G. Ramalingam, S. Raghavan and A. Ghosh, *Nat. Nanotechnol.*, 2013, **8**, 826–830.
40 H. Murata and A. Koma, *Phys. Rev. B: Condens. Matter Mater. Phys.*, 1999, **59**, 10327–10334.
41 A. Ramasubramaniam, *Phys. Rev. B: Condens. Matter Mater. Phys.*, 2012, **86**, 115409.
42 A. Castellanos-Gomez, N. Agraït and G. Rubio-Bollinger, *Appl. Phys. Lett.*, 2010, **96**, 213116.
43 M. M. Benameur, B. Radisavljevic, J. S. Héron, S. Sahoo, H. Berger and A. Kis, *Nanotechnology*, 2011, **22**, 125706.
44 P. Tonndorf, R. Schmidt, P. Bottger, X. Zhang, J. Borner, A. Liebig, M. Albrecht, C. Kloc, O. Gordan, D. R. T. Zahn, S. M. de Vasconcellos and R. Bratschitsch, *Opt. Express*, 2013, **21**, 4908–4916.
45 H. T. Wang, D. S. Kong, P. Johanes, J. J. Cha, G. Y. Zheng, K. Yan, N. A. Liu and Y. Cui, *Nano Lett.*, 2013, **13**, 3426–3433.
46 D. S. Kong, H. T. Wang, J. J. Cha, M. Pasta, K. J. Koski, J. Yao and Y. Cui, *Nano Lett.*, 2013, **13**, 1341–1347.
47 G. Cunningham, M. Lotya, C. S. Cucinotta, S. Sanvito, S. D. Bergin, R. Menzel, M. S. P. Shaffer and J. N. Coleman, *ACS Nano*, 2012, **6**, 3468–3480.
48 A. R. Beal and H. P. Hughes, *J. Phys. C: Solid State Phys.*, 1979, **12**, 881–890.
49 L. M. Smith, D. R. Wake, J. P. Wolfe, D. Levi, M. V. Klein, J. Klem, T. Henderson and H. Morkoç, *Phys. Rev. B: Condens. Matter Mater. Phys.*, 1988, **38**, 5788–5791.
50 R. Fivaz and E. Mooser, *Phys. Rev.*, 1967, **163**, 743–755.
51 A. Rettenberger, P. Leiderer, M. Probst and R. Haight, *Phys. Rev. B: Condens. Matter Mater. Phys.*, 1997, **56**, 12092–12095.